iScience

CellPress
OPEN ACCESS

Article

Biomineralization-inspired synthesis of autologous cancer vaccines for personalized metallo-immunotherapy

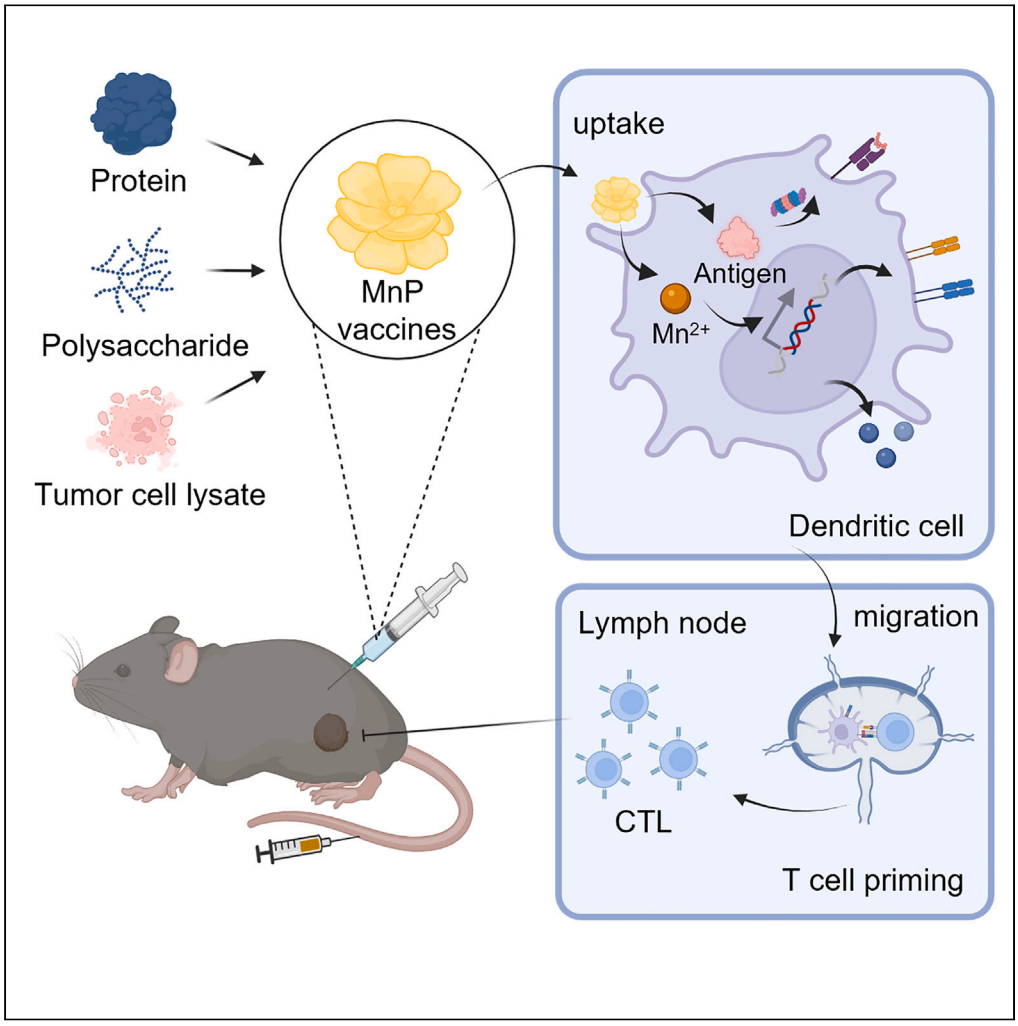

Quguang Li, Yifan Yan, Chunjie Wang, ..., Minming Chen, Zhuang Liu, Liangzhu Feng

lzfeng@suda.edu.cn

Highlights

A general biomineralization strategy is developed to encapsulate different antigens

The biomineralized autologous cancer vaccine elicits tumor-specific T cell responses

The autologous vaccine together with ICB therapy inhibits postsurgical tumor relapse

Li et al., iScience 27, 110189
July 19, 2024
https://doi.org/10.1016/j.isci.2024.110189

iScience

CellPress
OPEN ACCESS

Article

Biomineralization-inspired synthesis of autologous cancer vaccines for personalized metallo-immunotherapy

Quguang Li,[1,2] Yifan Yan,[1,2] Chunjie Wang,[1] Ziliang Dong,[1] Yu Hao,[1] Minming Chen,[1] Zhuang Liu,[1] and Liangzhu Feng[1,3,*]

SUMMARY

Autologous cancer vaccines represent a promising therapeutic approach against tumor relapse. Herein, a concise biomineralization strategy was developed to prepare an immunostimulatory autologous cancer vaccine through protein antigen-mediated growth of flower-like manganese phosphate (MnP) nanoparticles. In addition to inheriting the cyclic guanosine monophosphate-adenosine monophosphate synthase (cGAS)-stimulator of interferon genes (STING)-activating capacity of Mn^{2+}, the resulting ovalbumin (OVA)-loaded MnP (OVA@MnP) nanoparticles with superior stability and pH-responsiveness enabled efficient priming of antigen-specific $CD8^+$ T cell expansion through promoting the endo/lysosome escape and subsequent antigen cross-presentation of OVA. Resultantly, OVA@MnP vaccines upon subcutaneous vaccination elicited both prophylactic and therapeutic effects against OVA-expressing B16-F10 melanoma. Furthermore, the biomineralized autologous cancer vaccines prepared from the whole tumor cell lysates of the dissected tumors suppressed the growth of residual tumors, particularly in combination with anti-PD-1 immunotherapy. This study highlights a simple biomineralization approach for the controllable synthesis of cGAS-STING-activating autologous cancer vaccines to suppress postsurgical tumor relapse.

INTRODUCTION

The construction of effective cancer vaccines is a promising approach for preventing tumor relapse because it is highly effective at eliciting an antigen-specific tumor-eradicating immune response.[1–4] Because of the limited immunogenicity of most currently used protein- and peptide-associated antigens, various immune adjuvants have been introduced to facilitate the elicitation of antitumor immune responses by functioning as delivery vehicles and/or immunostimulatory agonists.[5–7] Although clinically used emulsions and aluminum salt-based vehicles can generate a depot of antigens and agonists at the injection site to benefit their sustainable release, these antigens still suffer from limited internalization and cross-presentation by dendritic cells (DCs), which are responsible for the priming of antigen-specific $CD8^+$ T cell responses.[5,8,9] Inspired by their potent capacity for molecular loading and cellular internalization, various synthetic and bioderived nanomaterials have been intensively explored for the development of cancer vaccines.[10–12] However, the distinctive physicochemical properties of tumor antigens and immunostimulatory agonists (e.g., solubility and molecular weights) often hinder their concurrent encapsulation at optimal ratios.[13–15] Therefore, there is an urgent need to develop innovative delivery carriers enabling tunable molecular loading and $CD8^+$ T cell response priming for the construction of highly efficient cancer vaccines.

Recently, stimulation of the cGAS-STING pathway with suitable agonists has been shown to be a robust approach for enhancing antitumor potency due to its essential role in both cancer and immune cells as an innate immune sensor.[16–19] It thereby effectively suppresses tumor progression by inducing cancer cell senescence and promoting tumor infiltration of various immune cells (e.g., T cells and natural killer cells) by upregulating the downstream secretion of type I interferons (IFNs) and other inflammatory factors.[20,21] Therefore, various cGAS-STING agonists, including free cyclic dinucleotides (CDNs), Mn^{2+} ions and pH-responsive polycations, have been developed and demonstrated to be promising candidates for effective cancer immunotherapy.[22–26] Furthermore, due to the superior potency of the activation of the cGAS-STING pathway in mediating the cross-priming of antigen-specific $CD8^+$ T cells, the rational development of cGAS-STING activating nano- and microparticles represents a promising approach for developing next-generation cancer vaccines because they can also benefit the internalization of tumor antigens.

[1]Institute of Functional Nano & Soft Materials (FUNSOM), Jiangsu Key Laboratory for Carbon-Based Functional Materials and Devices, Soochow University, 199 Ren' ai Road, Suzhou, Jiangsu 215123, P.R. China
[2]These authors contributed equally
[3]Lead contact
*Correspondence: lzfeng@suda.edu.cn
https://doi.org/10.1016/j.isci.2024.110189

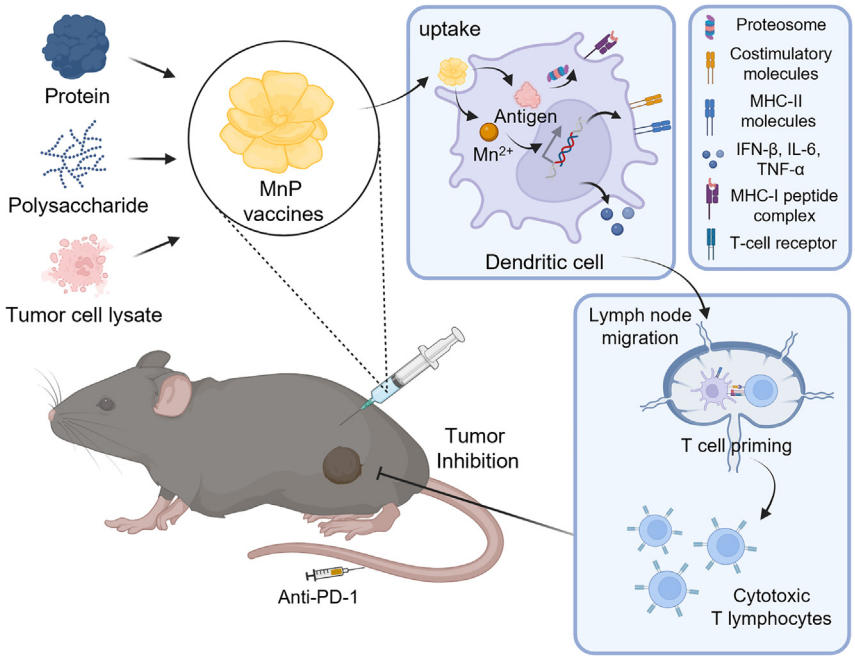

Figure 1. Schematic illustration of the biomineralization approach used to prepare a cGAS-STING-activating MnP-based vaccine and the mechanisms by which this approach induces potent cellular antitumor immunity

Various antigens, including proteins, polysaccharides, and TCLs, can be utilized to construct corresponding MnP vaccines. Due to the pH responsiveness of MnP, the as-prepared vaccines internalized by DCs could promote endo/lysosome escape of antigens and thus concurrently elicit a cross-primed antigen-specific cellular immune response to prevent tumor relapse, particularly in combination with anti-PD-1 immunotherapy.

Biomineralization, a process of coating organic matrices with inorganic minerals, has attracted extensive attention in the construction of functional biomedical materials.[27–29] In addition to conferring the controllable release of bioactive payloads, such a biomineralization process could also prevent them from being damaged by inappropriate environmental circumstances.[30,31] For example, it has been reported that *in situ* growth of a thin calcium phosphate shell on the surface of a virus can markedly improve its thermostability and immunogenicity,[32,33] and these silicified tumor vaccines obtained through cryogenic silicification of tumor cells can preserve their vaccination efficacy after long-term storage at room temperature.[34] However, these calcium phosphate- and silica-based biominerals possess only limited immunostimulatory capacity, which is important for priming potent adaptive immune responses.

Therefore, in this study, we proposed a concise biomineralization strategy to prepare cGAS-STING-activating autologous cancer vaccines via tumor lysate-templated growth of manganese phosphate (MnP) nanoparticles (Figure 1). This biomineralization approach was shown to encapsulate various proteins, yielding flower-like MnP nanoparticles with significantly improved stability. With OVA as the modeling antigen, the obtained OVA@MnP with both pH responsiveness and a cGAS-STING activating capacity promoted the cross-priming of OVA-specific $CD8^+$ T cells upon subcutaneous vaccination. As a result, upon subcutaneous vaccination, these OVA@MnP nanovaccines elicited more profound prophylactic and therapeutic effects against OVA-expressing B16-F10 melanoma than did bolus vaccination with free Mn^{2+} and CpG as immunostimulants. Furthermore, the autologous MnP nanovaccine with tumor cell lysates (TCLs) of resected tumors as the antigen could effectively inhibit the growth of residual tumors after incomplete surgical resection when it was concurrently applied with programmed cell death protein 1 antibody (anti-PD-1) immunotherapy. This study highlighted that such a biomineralization approach is a promising yet concise strategy for developing autologous cancer vaccines to prevent postsurgical tumor relapse.

RESULTS

Biomineralization synthesis of OVA@MnP

Biomacromolecules have been intensively explored as templates to guide the formation of biominerals because they can adsorb various metal ions via different mechanisms to form small protein-metal ion complexes, which can function as nucleation sites for biominerals.[28,35,36] Inspired by the high potency of Mn^{2+} in activating the cGAS-STING pathway by significantly promoting the synthesis of cGAMP and its binding with STING,[37,38] herein, a biomineralization approach was developed to prepare a protein-based cancer vaccine by encapsulating antigens with MnP nanoparticles (Figure 2A). By sequentially adding manganese chloride ($MnCl_2$) and sodium phosphate (Na_3PO_4) solutions to different concentrations of OVA solution utilized as a model protein antigen, the obtained OVA@MnP nanoparticles displayed a unique flower-like morphology under scanning electron microscopy (SEM) (Figure S1). Notably, OVA@MnP nanoparticles synthesized in the presence of 10 mg/mL OVA exhibited an average diameter of ~700 nm, which was much smaller than those of OVA@MnP prepared at lower

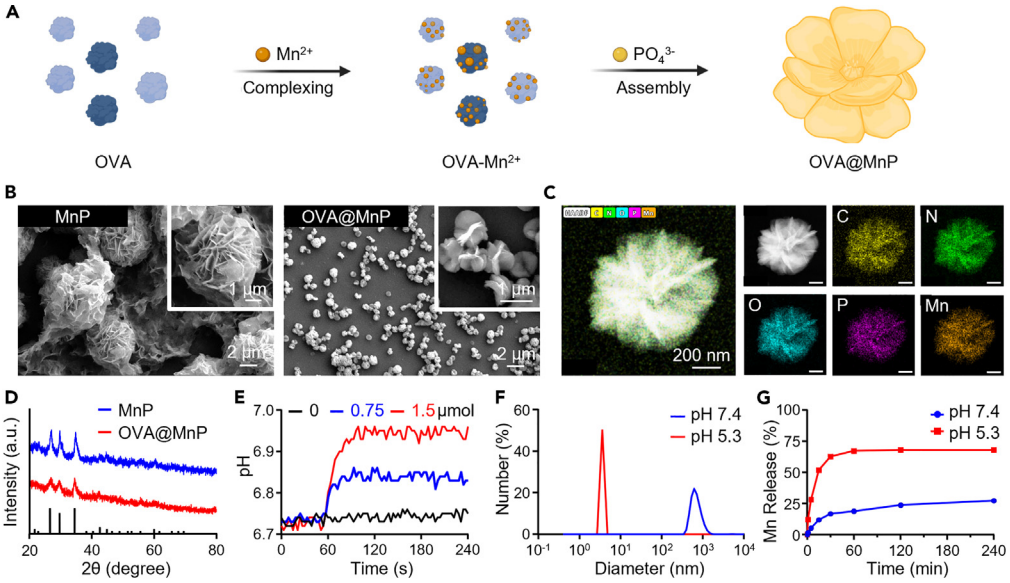

Figure 2. Synthesis and characterization of OVA@MnP nanoflowers

(A) A scheme demonstrating the synthetic procedures for OVA@MnP nanoflowers.

(B) Representative SEM images of MnP microparticles and OVA@MnP nanoflowers. The insets are their magnified images.

(C) STEM mapping imaging of the OVA@MnP nanoflower (scale bar, 200 nm).

(D) XRD patterns of the MnP and OVA@MnP nanoflowers.

(E) *In vitro* proton-neutralizing profiles of OVA@MnP.

(F) Hydrodynamic size distribution profiles of OVA@MnP nanoflowers incubated in buffer solutions at different pH values for 4 h before DLS measurements.

(G) Time-dependent release curves of Mn^{2+} from OVA@MnP nanoflowers incubated in different pH buffer solutions.

OVA concentrations and 6.8 ± 1.0 μm of the pure MnP particles prepared by directly mixing $MnCl_2$ with Na_3PO_4 in the absence of OVA (Figures 2B and S2). The smaller size of such OVA@MnP nanoparticles could be attributed to the ability of OVA to chelate Mn^{2+} to form large amounts of protein-metal ion nanocomplexes, which function as nucleation sites for the growth of separate petals according to previous studies.[27,39]

Via dynamic light scattering, OVA@MnP nanoparticles exhibited comparable size distribution profiles (676.8 nm to 703.9 nm) and slight negative surface charges (−0.188 mV to −1.770 mV) upon immersion in water, saline, and cell culture media (Table S1), indicating their excellent stability in physiological solutions. Via a bicinchoninic acid (BCA) assay, the loading efficiency of OVA in OVA@MnP was determined to be 9.96%, while it was 96.3% for Mn via a sodium periodate oxidation colorimetric assay.[40] The successful incorporation of OVA into OVA@MnP nanoparticles was also evidenced by the presence of nitrogen signals in the energy dispersive X-ray (EDX) elemental mapping images recorded by a scanning transmission electron microscope (TEM) (Figure 2C). By recording their X-ray diffraction (XRD) signals, OVA@MnP nanoparticles and plain MnP microparticles showed the same characteristic diffraction peaks at 2θ values of 26.586°, 29.655°, and 34.466°, which are consistent with those of $Mn_3(PO_4)_2 \cdot 3H_2O$ (JCPDS No. 03–0426) in terms of peak positions and peak intensity (Figure 2D).

Both bovine serum albumin (BSA, 10 mg/mL) and transferrin (10 mg/mL) could also be utilized as templates to promote the formation of corresponding flower-like particles (Figures S3A and S3B). In addition, we found that heparin sodium (0.1 mg/mL), a negatively charged polysaccharide, could also guide the formation of similar flower-like MnP particles via the aforementioned procedure (Figure S3C). Furthermore, it was discovered that such OVA@MnP retained its original morphology and showed good dispersity after being treated by autoclaving (121°C, 20 min) and lyophilization (Figures S4A and S4B). The OVA@MnP remained intact after storage under supercooling (−80°C), room temperature (25°C), or hyperthermia (60°C) conditions for up to 6 months (Figures S4C and S4D), while the MnP particles immediately collapsed upon freezing treatment (Figure S5). These results collectively indicate that such a biomineralization strategy is a concise yet general approach for encapsulating different types of biomacromolecules for the construction of corresponding vaccines with excellent stability.

Thereafter, by recording the pH values using a commercial pH microelectrode, we found that OVA@MnP could rapidly neutralize the acidic solution in a dose-dependent manner, indicating its excellent capacity to react with protons (Figure 2E). The hydrodynamic diameter of OVA@MnP also dramatically decreased from 712.7 nm to 3.6 nm after incubation with phosphate-buffered saline (PBS) at pH 5.3 for 4 h (Figure 2F). As a result, OVA@MnP exhibited pH-dependent release of Mn^{2+}, with 68.0% and 27.6% of the Mn^{2+} released after incubation at pH 5.3 and 7.4 for 4 h, respectively (Figure 2G). OVA@MnP also showed similar pH-dependent release of OVA (Figure S6). Collectively, these results indicate the excellent pH-responsive dissociation capacity of OVA@MnP.

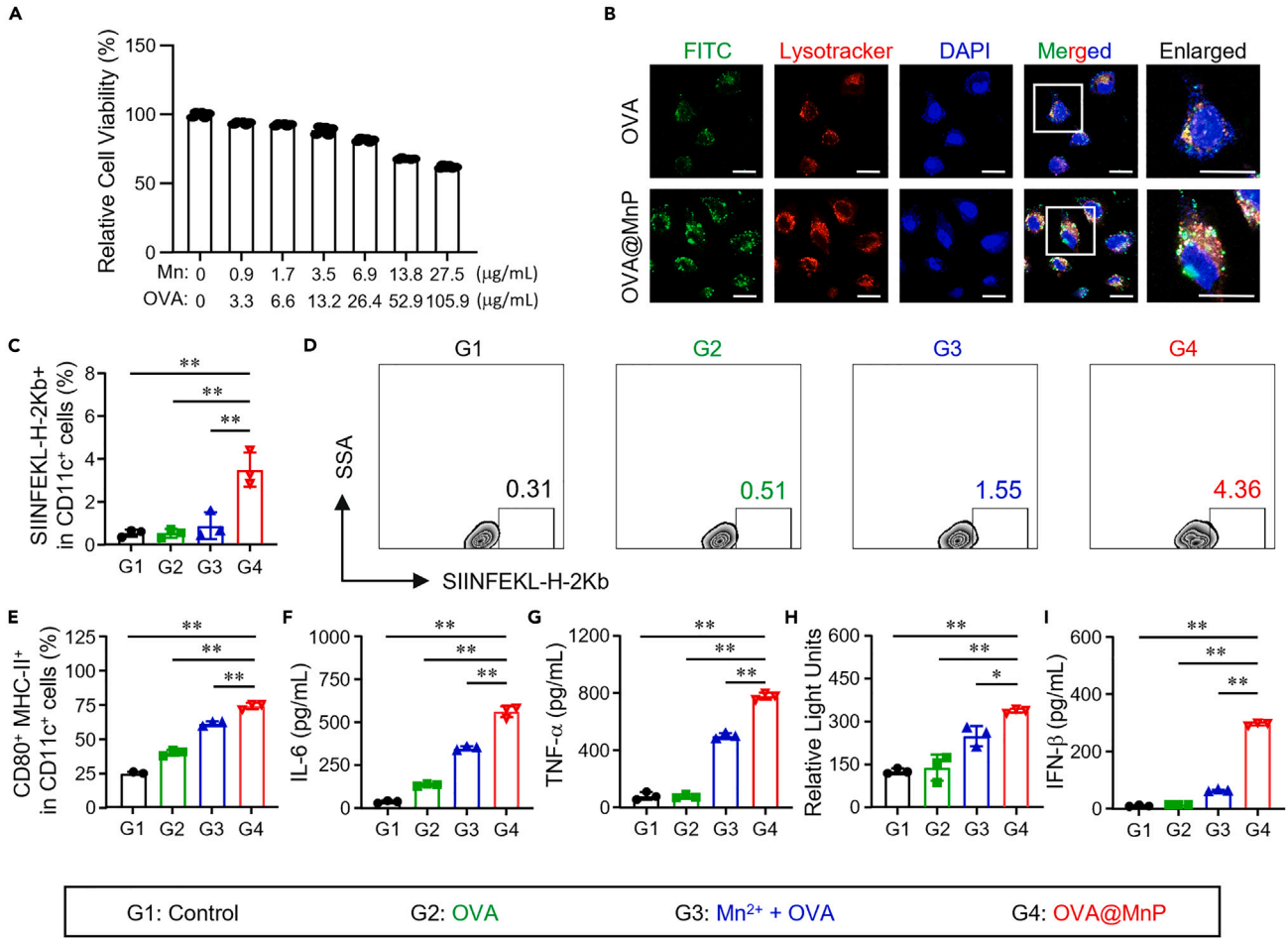

Figure 3. *In vitro* cellular experiments

(A) Relative cell viability of DC2.4 cells after incubation with OVA@MnP at different concentrations for 24 h (n = 6).

(B) Confocal fluorescence images of DC2.4 cells incubated with FITC-labeled OVA or OVA@MnP for 6 h (scale bar, 20 μm).

(C) Flow cytometry analysis of the presentation levels of the SIINFEKL-H-2Kb complex on the surface of DCs after the indicated treatments (n = 3) and D) corresponding representative flow cytometry patterns.

(E) Flow cytometry analysis of the maturation levels of BMDCs after different treatments for 24 h as indicated (n = 3).

(F and G) Secretion levels of IL-6 (f) and TNF-α (g) by BMDCs after different treatments were quantified by using corresponding ELISA kits (n = 3).

(H) Bioluminescence intensities of cGAS plasmid-transfected 293-Dual HEK mSTING cells after different treatments for 24 h as indicated (n = 3).

(I) IFN-β secretion levels of BMDCs after different treatments quantified by ELISA (n = 3). Data are presented as the mean ± s.d. Statistical significance between the indicated groups was calculated by using two-tailed Student's t tests. *p < 0.05, **p < 0.01.

In vitro cGAS-STING activation and antigen cross-presentation capacity of OVA@MnP

We first evaluated the biocompatibility of OVA@MnP in the murine dendritic cell line DC2.4 via the standard 3-(4,5-dimethyl-2-thiazolyl)-2,5-diphenyl-2-H-tetrazolium bromide (MTT) assay. The viability of DC2.4 cells incubated with OVA@MnP at a Mn^{2+} concentration of 6.9 μg/mL for 24 h was 88.7% (Figure 3A), indicating the suitable biocompatibility of OVA@MnP under the tested conditions. Similar results were also obtained in the murine embryonic fibroblast line NIH-3T3 (Figure S7). We then carefully investigated the intracellular trafficking behavior of OVA@MnP, in which OVA was prelabeled with fluorescein isothiocyanate (FITC), via confocal microscopy. After incubation with FITC-labeled OVA@MnP (Mn = 3.5 μg/mL; OVA = 13.2 μg/mL) for 6 h, DC2.4 cells exhibited strong punctate green fluorescence of FITC, which was not fully colocalized with the fluorescence of LysoTracker red, a commercial pH-sensitive fluorescent dye used to label lysosomes (Figure 3B). In marked contrast, DC2.4 cells incubated with OVA-FITC under the same conditions only displayed a weaker intracellular FITC fluorescence signal. According to the results of the ImageJ analysis, the Pearson correlation coefficient of OVA@MnP-treated DC2.4 cells was determined to be 0.80 ± 0.02, which was significantly lower than the 0.87 ± 0.03 for OVA-treated cells (Figure S8). These results revealed that OVA@MnP significantly promoted the endocytotic and endo-/lysosomal escape of OVA.

Furthermore, via flow cytometry, it was discovered that murine bone marrow-derived dendritic cells (BMDCs) incubated with OVA@MnP (Mn = 3.5 μg/mL; OVA = 13.2 μg/mL) for 24 h exhibited obviously increased binding of SIINFEKL, a representative peptide epitope of OVA, to

the H-2Kb of MCH-I (Figures 3C and 3D). In sharp contrast, treatment of these BMDCs with bare OVA or Mn^{2+} plus OVA exhibited a negligible impact on the expression of SIINFEKL-H-2Kb, indicating the high capacity of OVA@MnP to enable the cross-presentation of OVA. We then investigated the immunostimulatory capacity of OVA@MnP. By flow cytometry, we found that incubation with OVA@MnP effectively promoted the expression of the costimulatory molecules CD80 and major histocompatibility complex (MHC) class II (MHC-II) on the surface of BMDCs (Figures 3E and S9). In contrast, treatments with bare OVA or Mn^{2+} plus OVA were less effective at promoting the expression of these costimulatory molecules. Moreover, through enzyme-linked immunosorbent assay (ELISA), incubation with OVA@MnP was also shown to be the most effective at promoting the secretion of interleukin (IL)-6 and tumor necrosis factor-alpha (TNF-α) by BMDCs (Figures 3F and 3G). These results collectively indicate the high capacity of OVA@MnP to promote the maturation of DCs.

Mn^{2+} can stimulate the cGAS-STING pathway to promote DC maturation and the secretion of diverse downstream proinflammatory cytokines (e.g., IFN-β).[41–43] We then explored the capacity of OVA@MnP to activate the cGAS-STING pathway via a series of standard characteristic experiments. It has been well documented that cGAS-transfected 293-Dual mSTING reporter cells (ISG-SEAP/KI-[IFN-β]Lucia) can activate STING by secreting Lucia luciferase in place of IFN-β.[44] Therefore, upon incubation with OVA@MnP (Mn = 3.5 μg/mL; OVA = 13.2 μg/mL), these cells were capable of emitting bioluminescence upon the addition of coelenterazine, the substrate of Lucia luciferase (Figure 3H). In contrast, treatment with Mn^{2+} plus OVA markedly reduced the capacity to promote the emission of bioluminescence under the same experimental conditions. Moreover, via ELISA, we found that incubation with OVA@MnP was also the most effective at stimulating the secretion of IFN-β by BMDCs (Figure 3I), collectively indicating the highly effective capacity of OVA@MnP to activate cGAS-STING.

In vivo vaccination capacity of OVA@MnP

Motivated by the efficient cGAS-STING activation and antigen cross-presentation performance of OVA@MnP, its ability to elicit an antigen-specific cellular immune response was investigated in C57BL/6 mice. To this end, five groups (n = 5) of healthy mice were treated as follows: group 1, saline; group 2, OVA; group 3, CpG-ODN + OVA; group 4, Mn^{2+} + OVA; and group 5, OVA@MnP. CpG-ODN, a clinically approved Toll-like receptor 9 (TLR-9) agonist for cancer immunotherapy, was adopted as a positive control in this study due to its high capacity to facilitate the elicitation of cytotoxic T lymphocyte (CTL) immunological responses according to previous studies.[45–47] These mice received corresponding subcutaneous (s.c.) injections once a week three times, and the injection doses of OVA, Mn^{2+} and CpG were 5.6 mg/kg, 1.5 mg/kg, and 1 mg/kg, respectively. (Figure 4A). Then, these mice were sacrificed, and their serum, inguinal lymph nodes (iLNs) and spleens were collected for immune analysis seven days after the last vaccination. It was first found that vaccination with OVA@MnP resulted in the effective recruitment of $CD11c^+$ DCs and their maturation inside iLNs with efficacy comparable to that of vaccination with CpG-ODNs and OVA (Figures 4B, 4C, S10, and S11). In contrast, vaccination with OVA alone or with Mn^{2+} + OVA was less effective at promoting the recruitment and maturation of DCs. In addition, vaccination with OVA@MnP promoted the expression of SIINFEKL-H-2Kb on the surface of DCs inside iLNs with efficacy comparable to that of CpG-ODN and OVA treatment (Figures 4D and S12).

Thereafter, we investigated the ability of OVA@MnP vaccines to elicit OVA-specific $CD8^+$ T cells. The flow cytometry results revealed that the splenocyte fraction of the mice vaccinated with OVA@MnP was greater (2.35 ± 0.98%) among the SIINFEKL-MHC-I tetramer$^+$$CD8^+$ T cells than that of the other groups, while that of the mice treated with CpG-ODN + OVA was 1.43 ± 0.20%, although the difference was not statistically significant (Figures 4E, 4F, and S13). Consistently, vaccination with OVA alone or with Mn^{2+} + OVA was also less effective at eliciting OVA-specific tetramer$^+$$CD8^+$ T cells. Moreover, vaccination with OVA@MnP also led to effective activation of $CD8^+$ T cells, indicated by a fraction of 1.48 ± 0.52% of $CD8^+$ T cells expressing interferon-gamma (IFN-$\gamma^+$$CD8^+$ T cells) inside the splenocyte population, as determined by flow cytometry (Figures 4G and 4H). Vaccination with CpG-ODNs and OVA only led to the activation of 0.86 ± 0.18% of IFN-$\gamma^+$$CD8^+$ T cells. The high capacity of OVA@MnP vaccination to boost the activation of effector $CD8^+$ T cells was further confirmed by recording IFN-γ spot-forming cells using an enzyme-linked immune absorbent spot (ELISPOT) (Figure 4G–4I and S14). Taken together, these results demonstrate that OVA@MnP is capable of eliciting effective antigen-specific $CD8^+$ T cell responses.

Prophylactic and therapeutic vaccination effect of OVA@MnP

Motivated by the high potency of OVA@MnP in eliciting an OVA-specific cellular immune response, we first evaluated the capacity of OVA@MnP vaccination to elicit a prophylactic immune response against OVA-expressing B16 (B16-OVA) melanoma. To this end, another 5 groups of healthy C57BL/6 mice receiving the same triplicate s.c. injections as mentioned previously were challenged with B16-OVA melanoma via s.c. inoculation seven days after the final immunization (Figure 5A). Vaccination with OVA@MnP was capable of suppressing the growth of B16-OVA melanoma (Figures 5B and 5C), and these mice exhibited a median survival time of 34 days (Figure 5D). In contrast, the median survival times of mice vaccinated with bolus injections of OVA + CpG-ODN or OVA + Mn^{2+} were 24 days and 22 days, respectively, while that for mice not receiving vaccination was 18 days. In addition, we did not observe any significant weight loss during the entire experimental period (Figure S15). Taken together, these results demonstrate that OVA@MnP can elicit effective prophylactic immune responses.

We then compared the tumor inhibition efficacies of such OVA-MnP vaccines with those of traditional bolus injections of OVA and other immunostimulatory agents in a B16-OVA melanoma model. To this end, five groups of healthy C57BL/6 mice were first s.c. inoculated with B16-OVA at 4 days before being subjected to s.c. vaccinations with the same triplicate injections as mentioned previously (Figure 5E). By recording tumor sizes, it was also found that vaccination with OVA@MnP was also the most effective at suppressing the growth of B16-OVA melanoma, and the median survival time of these mice was determined to be 28 days. In marked contrast, the OVA + CpG-ODN or OVA + Mn^{2+} combination had only slight therapeutic efficacy, and the median survival times of these two groups of mice were only

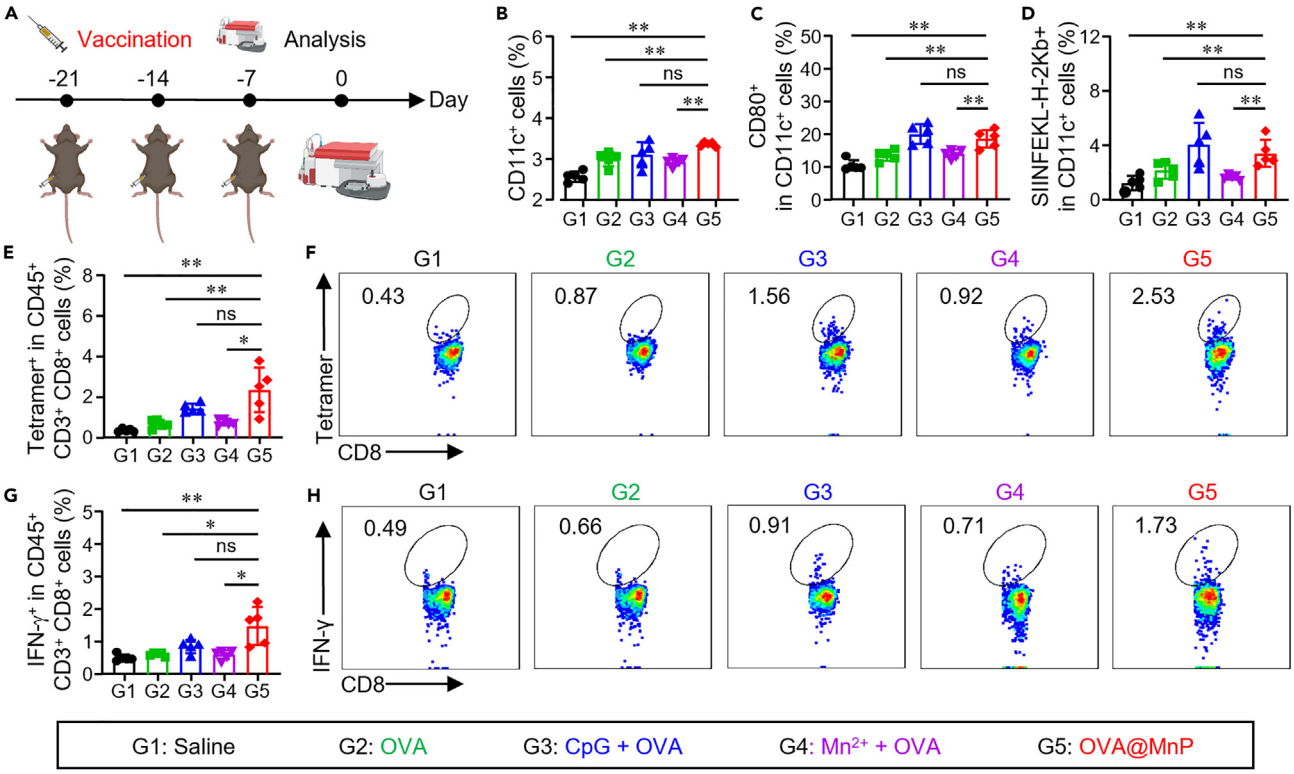

Figure 4. *In vivo* vaccination performance of OVA@MnP

(A) Schematic illustration of the experimental schedule.

(B–D) Flow cytometric analysis of DC percentages (B), DC maturation levels (C) and OVA cross-presentation levels in the inguinal lymph nodes of C57BL/6 mice given the indicated treatments.

(E) Statistical analysis and (F) representative flow cytometric patterns of the frequency of SIINFEKL-H-2Kb tetramer$^+$ cells among CD45$^+$CD3$^+$CD8$^+$ T cells in the spleens of mice subjected to the indicated treatments.

(G) Statistical analysis and (H) representative flow cytometric patterns showing the percentage of IFN-γ$^+$-expressing CD45$^+$CD3$^+$CD8$^+$ T cells in restimulated splenocytes. Statistical significance between the indicated groups was calculated by using two-tailed Student's t tests. *$p < 0.05$, **$p < 0.01$.

20 days and 22 days, respectively (Figures 5F and 5G). Furthermore, the body weights of all treated mice showed minimal fluctuations (Figure S16). These results collectively indicate the great promise of OVA@MnP as a therapeutic cancer vaccine.

Combined TCL@MnP vaccine and anti-PD-1 to suppress postsurgical tumor relapse

Surgical resection is still a mainstream strategy for treating almost all solid tumors, but patients, particularly those with advanced tumors, are prone to tumor relapse.[48–50] Motivated by the robustness of our developed biomineralization strategy for encapsulating different types of biomacromolecules, we investigated the feasibility of preparing an autologous cancer vaccine with TCLs via such a biomineralization approach to inhibit postsurgical tumor relapse. To this end, B16-F10 melanoma tissue from C57BL/6 mice (100 mm^3) was first incompletely excised, with ~5% of the tumor mass remaining as the residual tumor model, and the excised tumor mass was then prepared into the corresponding TCLs by successive heat deactivation and urea lysis under sonication. Notably, SEM imaging revealed that the B16-TCLs with 95°C pre-treatment for 10 min led to the formation of more uniform flower-like B16-TCL@MnP particles compared to these prepared from the as-prepared B16-TCLs without 95°C pre-treatment (Figure S17). Then, the mice bearing residual B16-F10 tumors were randomly divided into four groups and received different treatments as follows: group 1, saline; group 2, anti-PD-1; group 3, B16-TCL@MnP; and group 4, B16-TCL@MnP + anti-PD-1. B16-TCL@MnP was s.c. injected into the left ventral flank of mice at 1, 8, and 15 days after tumor excision three times, while anti-PD-1 was administered intravenously at 2 and 5 days after each B16-TCL@MnP vaccination (Figure 6A).

By recording tumor sizes, we found that the combination treatment of B16-TCL@MnP vaccination plus anti-PD-1 immunotherapy demonstrated the most effective potency in suppressing the growth of residual tumors (Figures 6C and 6D). The median survival time of the mice in this group was 26 days, and 3 of the 7 mice were fully cured without recurrence for up to 60 days (Figure 6E). In sharp contrast, monotherapy with anti-PD-1 immunotherapy or B16-TCL@MnP vaccination had only moderate inhibitory effects on these residual tumors, and the median survival times of mice receiving these two treatments were 12 days and 16 days, respectively, which were only slightly longer than 10 days for mice not receiving the corresponding treatment. Additionally, no obvious weight loss was observed for the mice that received various treatments throughout the entire monitoring period (Figure S18). In addition, we further validated the effectiveness of this strategy in inhibiting

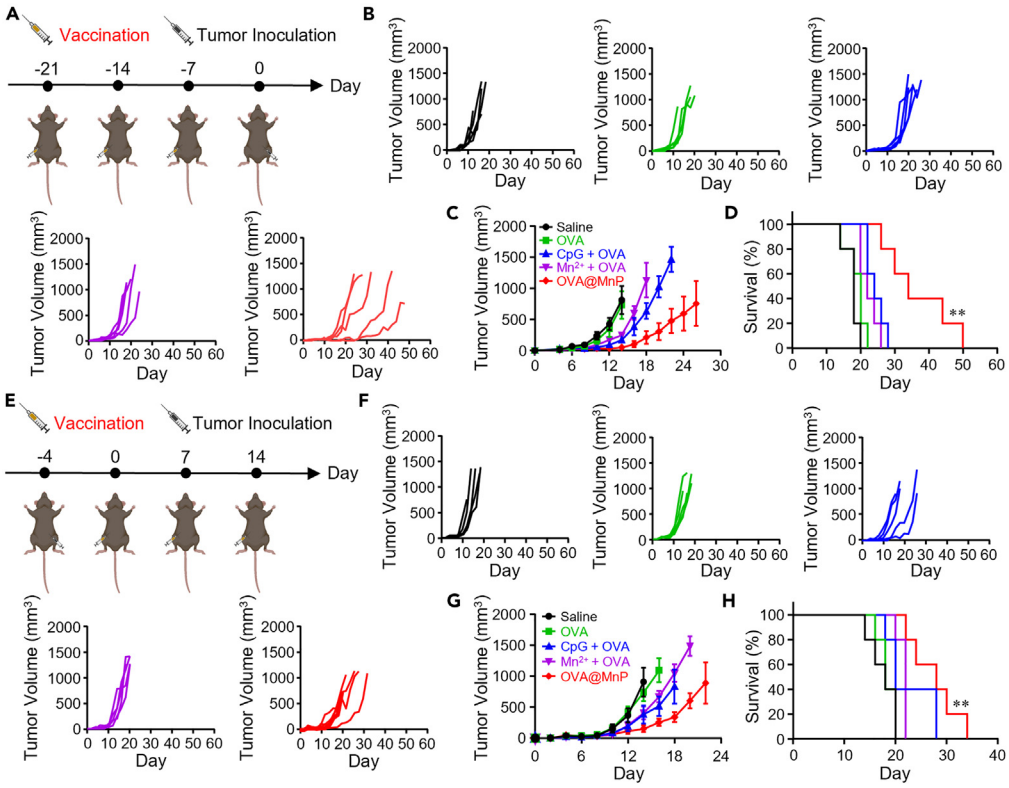

Figure 5. *In vivo* prophylactic and therapeutic potencies of OVA@MnP nanoflowers

(A) Scheme illustrating the tumor challenge experimental schedule used to evaluate the prophylactic effects of OVA@MnP.

(B–D) Individual tumor growth curves (B), average tumor growth curves (C) and survival curves (D) of B16-OVA tumor-bearing mice after various prophylactic treatments as indicated (n = 5).

(E) Scheme illustrating the tumor challenge experimental schedule used to evaluate the therapeutic effects of OVA@MnP.

(F–H) Individual tumor growth curves (F), average tumor growth curves (G) and survival curves (H) of B16-OVA tumor-bearing mice after various therapeutic treatments as indicated (n = 5). Data are presented as the mean ± s.e.m. Survival curves were obtained using the Kaplan-Meier method and compared by the log rank test. **$p < 0.01$.

tumor recurrence in a murine CT26 colon tumor model. CT26-CTL@MnP prepared via the same procedure mentioned previously exhibited a similar flower-like morphology (Figure S19) and biocompatibility toward DC2.4 and NIH-3T3 cells (Figure S20) and could synergize with anti-PD-1 immunotherapy to effectively inhibit the growth of residual tumor masses (Figure 6F–6H and S21). Moreover, H&E staining of the major organs of the mice collected 21 days after the indicated treatments revealed no significant histological damage (Figure S22). Taken together, these results demonstrate that such a biomineralization approach is a concise strategy for preparing potent autologous cancer vaccines for the effective treatment of postoperative tumor relapse, particularly when combined with immune checkpoint blockade (ICB) immunotherapy.

DISCUSSION

Autologous cancer vaccines are promising tumor treatment modalities for preventing high-risk postsurgical tumor relapse, but their clinical therapeutic effectiveness is still unsatisfactory. Considering the importance of lymph node-targeted delivery of tumor antigens and immunostimulants in priming antitumor immunity, a series of particular delivery vehicles enabling efficient loading of both tumor antigens and immunostimulants have been widely explored to generate potent cancer vaccines. Inspired by the capacity of biomacromolecules to adsorb metal ions to form a large number of small complexes that can function as nucleation sites to facilitate the growth of biominerals, a biomineralization strategy has been shown to be robust for the construction of a new generation of cancer vaccines. This study rationally developed a biomineralization strategy to prepare a particular autologous cancer vaccine with a cGAS-STING activation capacity by utilizing whole TCLs as templates to guide the growth of flower-like MnP nanoparticles. In addition to TCLs, different pure proteins (e.g., OVA, transferrin, BSA) and polysaccharides (e.g., heparin) can also guide the generation of MnP particles with similar morphologies via biomineralization strategies, indicating that biomineralization is a general method for accessing different biomineralized cancer vaccines. Furthermore, it was shown that such MnP-based biomineralized cancer vaccines exhibited greatly improved stability, as indicated by their ability to maintain their original morphology after being subjected to autoclaving, lyophilization, and long-term storage under supercooling (−80°C), room temperature (25°C), or hyperthermia (60°C) conditions.

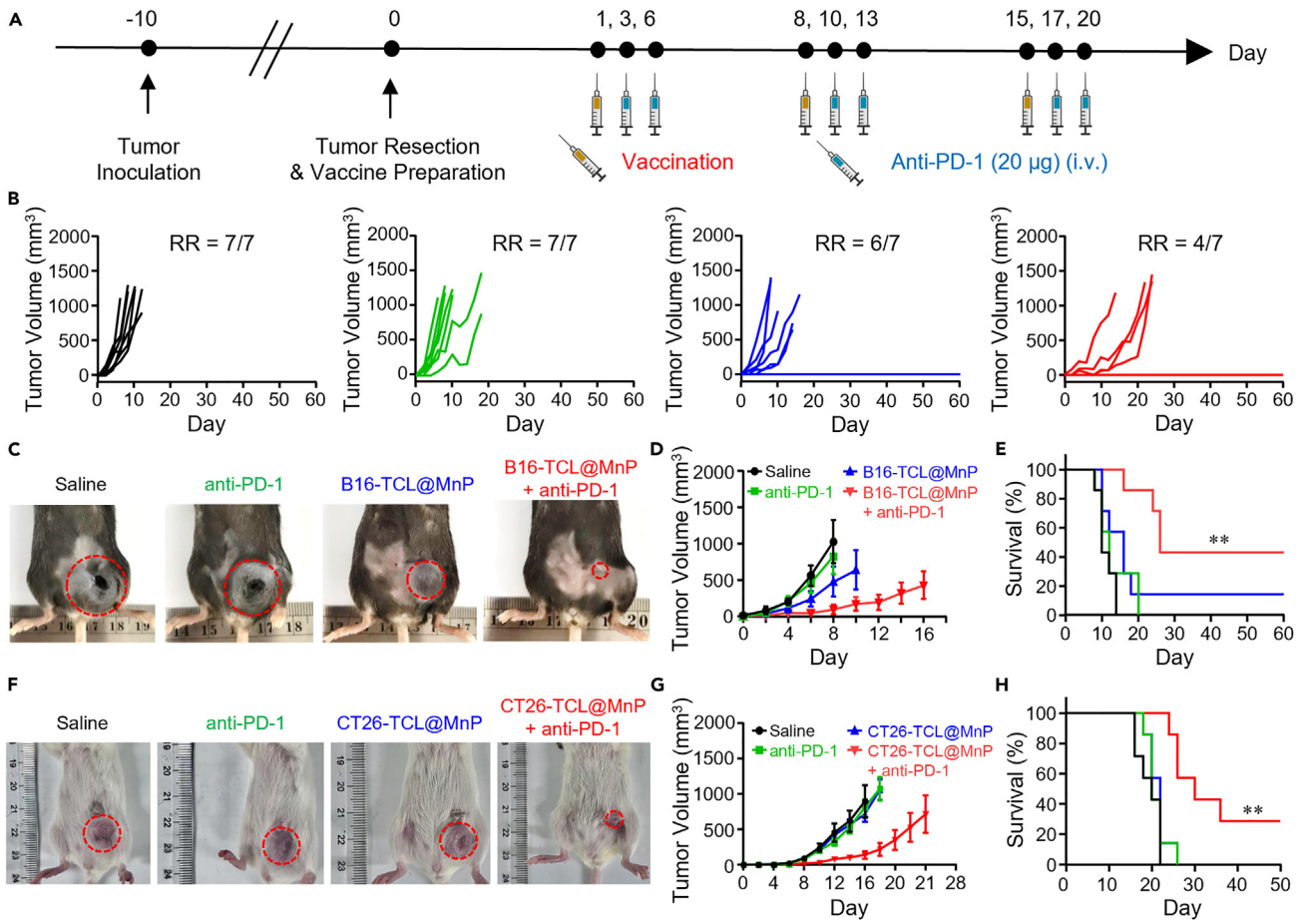

Figure 6. *In vivo* antitumor efficacy of combined TCL@MnP vaccination and anti-PD-1 immunotherapy

(A) A schematic illustration of the schedule used to evaluate the tumor relapse-inhibiting efficacy of combined B16-TCL@MnP vaccination and anti-PD-1 immunotherapy.

(B–E) Individual tumor growth curves (B), representative digital photographs (C), average tumor growth curves (D) and survival curves (E) of residual B16 tumor-bearing mice after various treatments ($n = 7$).

(F–H) Representative digital photographs (F), average tumor growth curves (G) and survival curves (H) of residual CT26 tumor-bearing mice after various treatments ($n = 7$). Data are presented as the mean ± s.e.m. Survival curves were obtained using the Kaplan-Meier method and compared by the log rank test. $^{**}p < 0.01$. RR, recurrence rate.

Efficient cross-presentation of exogenous proteinic tumor antigens is a prerequisite for eliciting tumor-specific cellular immunity for tumor eradication, and our OVA@MnP with pH-responsive dissociation capacity enabled efficient escape of OVA from endo-/lysosomes, a pivotal step in antigen cross-presentation. Together with the intrinsic capacity of cGAS-STING activation to facilitate the priming of cellular immune responses, OVA@MnP was capable of priming the OVA-specific $CD8^+$ T cell immune responses to suppress the growth of rechallenged tumors. Furthermore, vaccination with TCL@MnP was shown to inhibit the growth of residual tumor masses, in particular by synergizing with anti-PD-1 immunotherapy, which can protect tumor-infiltrating $CD8^+$ T cells from the immunosuppressive microenvironments of residual tumor masses. Considering that TCLs theoretically encompass entire tumor-specific antigenic epitopes, such a TCL@MnP vaccine holds great promise for enabling precise tumor suppression and could be prepared within one day without the time-consuming antigen screening period faced by neoantigen-based cancer vaccines.

In summary, this study highlights a concise yet potent biomineralization strategy to prepare effective autologous cancer vaccines with improved stability and cGAS-STING activating capacity. Combined with its excellent biocompatibility and simple preparation method, this autologous tumor vaccine holds great promise for future clinical translation.

Limitations of the study

We developed a biomineralization method to synthesis cGAS-STING activating particular autologous cancer vaccines for the suppression of post-surgical tumor relapse. However, there are still several limitations to this study. Although we have shown that the as-prepared OVA@MnP vaccines could maintain their original particular morphology under a variety of extreme conditions (e.g., autoclaved, lyophilized), the

vaccination capacity of these treated OVA-MnP remains to be further explored. In addition, we also need to further investigate the particle size, the ratio of Mn^{2+}/antigen, the vaccination dosages and some other properties of the vaccines to achieve maximal prophylactic and therapeutic effects. Moreover, it would be helpful to understand the detailed immunostimulatory mechanism of such vaccines at the *in vivo* level by using cGAS and STING knockout mouse models.

STAR★METHODS

Detailed methods are provided in the online version of this paper and include the following:

- KEY RESOURCES TABLE
- RESOURCE AVAILABILITY
  - Lead contact
  - Materials availability
  - Data and code availability
- EXPERIMENTAL MODEL AND STUDY PARTICIPANT DETAILS
  - Cell lines
  - Animals
- METHOD DETAILS
  - Synthesis and characterization of OVA@MnP
  - *In vitro* cell experiments
  - *In vivo* animal experiments
- QUANTIFICATION AND STATISTICAL ANALYSIS

SUPPLEMENTAL INFORMATION

Supplemental information can be found online at https://doi.org/10.1016/j.isci.2024.110189.

ACKNOWLEDGMENTS

This work was partially supported by the National Natural Science Foundation of China (22077093, 32322046), the National Research Programs from the Ministry of Science and Technology (MOST) of China (2021YFF0701800, 2022YFF0706500), the Natural Science Foundation of Jiangsu Province (BK20220110), the Collaborative Innovation Center of Suzhou Nano Science and Technology, the Suzhou Key Laboratory of Nanotechnology and Biomedicine, and the 111 Program from the Ministry of Education of China. We also thank the website of the Biorender.com for assisting in creating the illustrations.

AUTHOR CONTRIBUTIONS

Conceptualization, Q.L., Y.Y., Z.L., and L.F.; methodology and validation, Q.L., Y.Y., C.W., Z.D., Y.H., Z.L., and L.F.; investigation, Q.L., Y.Y., Y.H., M.C., and L.F.; writing – original draft, Q.L., Y.Y., C.W., and L.F.; writing – review and editing, Q.L., Q.C., and L.F.; supervision, Z.L. and L.F.; funding acquisition, L.F.

DECLARATION OF INTERESTS

The authors declare that they have no financial or other interests.

Received: March 11, 2024
Revised: May 3, 2024
Accepted: June 3, 2024
Published: June 5, 2024

REFERENCES

1. Wang, T., Wang, D., Yu, H., Feng, B., Zhou, F., Zhang, H., Zhou, L., Jiao, S., and Li, Y. (2018). A cancer vaccine-mediated postoperative immunotherapy for recurrent and metastatic tumors. Nat. Commun. *9*, 1532. https://doi.org/10.1038/s41467-018-03915-4.
2. Ye, X., Liang, X., Chen, Q., Miao, Q., Chen, X., Zhang, X., and Mei, L. (2019). Surgical tumor-derived personalized photothermal vaccine formulation for cancer immunotherapy. ACS Nano *13*, 2956–2968. https://doi.org/10.1021/acsnano.8b07371.
3. Saxena, M., van der Burg, S.H., Melief, C.J.M., and Bhardwaj, N. (2021). Therapeutic cancer vaccines. Nat. Rev. Cancer *21*, 360–378. https://doi.org/10.1038/s41568-021-00346-0.
4. Blass, E., and Ott, P.A. (2021). Advances in the development of personalized neoantigen-based therapeutic cancer vaccines. Nat. Rev. Clin. Oncol. *18*, 215–229. https://doi.org/10.1038/s41571-020-00460-2.
5. Li, W.-H., and Li, Y.-M. (2020). Chemical strategies to boost cancer vaccines. Chem. Rev. *120*, 11420–11478. https://doi.org/10.1021/acs.chemrev.9b00833.
6. Pulendran, B., O'Hagan, D.T., and O'Hagan, D.T. (2021). Emerging concepts in the science of vaccine adjuvants. Nat. Rev. Drug Discov. *20*, 454–475. https://doi.org/10.1038/s41573-021-00163-y.
7. Shi, S., Zhu, H., Xia, X., Liang, Z., Ma, X., and Sun, B. (2019). Vaccine adjuvants: Understanding the structure and mechanism of adjuvanticity. Vaccine *37*, 3167–3178.

https://doi.org/10.1016/j.vaccine.2019.04.055.
8. Li, H., Li, Y., Jiao, J., and Hu, H.-M. (2011). Alpha-alumina nanoparticles induce efficient autophagy-dependent cross-presentation and potent antitumour response. Nat. Nanotechnol. *6*, 645–650. https://doi.org/10.1038/nnano.2011.153.
9. Oleszycka, E., and Lavelle, E.C. (2014). Immunomodulatory properties of the vaccine adjuvant alum. Curr. Opin. Immunol. *28*, 1–5. https://doi.org/10.1016/j.coi.2013.12.007.
10. Aikins, M.E., Xu, C., and Moon, J.J. (2020). Engineered nanoparticles for cancer vaccination and immunotherapy. Acc. Chem. Res. *53*, 2094–2105. https://doi.org/10.1021/acs.accounts.0c00456.
11. Song, C., Li, F., Wang, S., Wang, J., Wei, W., and Ma, G. (2020). Recent advances in particulate adjuvants for cancer vaccination. Adv. Ther. *3*, 1900115. https://doi.org/10.1002/adtp.201900115.
12. Kroll, A.V., Jiang, Y., Zhou, J., Holay, M., Fang, R.H., and Zhang, L. (2019). Biomimetic nanoparticle vaccines for cancer therapy. Adv. Biosyst. *3*, 1800219. https://doi.org/10.1002/adbi.201800219.
13. Chen, F., Wang, Y., Gao, J., Saeed, M., Li, T., Wang, W., and Yu, H. (2021). Nanobiomaterial-based vaccination immunotherapy of cancer. Biomaterials *270*, 120709. https://doi.org/10.1016/j.biomaterials.2021.120709.
14. Shemesh, C.S., Hsu, J.C., Hosseini, I., Shen, B.-Q., Rotte, A., Twomey, P., Girish, S., and Wu, B. (2021). Personalized cancer vaccines: clinical landscape, challenges, and opportunities. Mol. Ther. *29*, 555–570. https://doi.org/10.1016/j.ymthe.2020.09.038.
15. Malonis, R.J., Lai, J.R., and Vergnolle, O. (2020). Peptide-based vaccines: current progress and future challenges. Chem. Rev. *120*, 3210–3229. https://doi.org/10.1021/acs.chemrev.9b00472.
16. Yan, J., Wang, G., Xie, L., Tian, H., Li, J., Li, B., Sang, W., Li, W., Zhang, Z., and Dai, Y. (2022). Engineering Radiosensitizer-Based Metal-Phenolic Networks Potentiate STING Pathway Activation for Advanced Radiotherapy. Adv. Mater. *34*, 2105783. https://doi.org/10.1002/adma.202105783.
17. Samson, N., and Ablasser, A. (2022). The cGAS–STING pathway and cancer. Nat. Cancer *3*, 1452–1463. https://doi.org/10.1038/s43018-022-00468-w.
18. Decout, A., Katz, J.D., Venkatraman, S., and Ablasser, A. (2021). The cGAS–STING pathway as a therapeutic target in inflammatory diseases. Nat. Rev. Immunol. *21*, 548–569. https://doi.org/10.1038/s41577-021-00524-z.
19. Li, S., Luo, M., Wang, Z., Feng, Q., Wilhelm, J., Wang, X., Li, W., Wang, J., Cholka, A., Fu, Y.-x., et al. (2021). Prolonged activation of innate immune pathways by a polyvalent STING agonist. Nat. Biomed. Eng. *5*, 455–466. https://doi.org/10.1038/s41551-020-00675-9.
20. Li, X., Khorsandi, S., Wang, Y., Santelli, J., Huntoon, K., Nguyen, N., Yang, M., Lee, D., Lu, Y., Gao, R., et al. (2022). Cancer immunotherapy based on image-guided STING activation by nucleotide nanocomplex-decorated ultrasound microbubbles. Nat. Nanotechnol. *17*, 891–899. https://doi.org/10.1038/s41565-022-01134-z.
21. Sun, X., Zhang, Y., Li, J., Park, K.S., Han, K., Zhou, X., Xu, Y., Nam, J., Xu, J., Shi, X., et al. (2021). Amplifying STING activation by cyclic dinucleotide–manganese particles for local and systemic cancer metalloimmunotherapy. Nat. Nanotechnol. *16*, 1260–1270. https://doi.org/10.1038/s41565-021-00962-9.
22. Van Herck, S., Feng, B., and Tang, L. (2021). Delivery of STING agonists for adjuvanting subunit vaccines. Adv. Drug Deliv. Rev. *179*, 114020. https://doi.org/10.1016/j.addr.2021.114020.
23. Garland, K.M., Sheehy, T.L., and Wilson, J.T. (2022). Chemical and biomolecular strategies for STING pathway activation in cancer immunotherapy. Chem. Rev. *122*, 5977–6039. https://doi.org/10.1021/acs.chemrev.1c00750.
24. Zhang, R., Wang, C., Guan, Y., Wei, X., Sha, M., Yi, M., Jing, M., Lv, M., Guo, W., Xu, J., et al. (2021). Manganese salts function as potent adjuvants. Cell. Mol. Immunol. *18*, 1222–1234. https://doi.org/10.1038/s41423-021-00669-w.
25. Luo, M., Wang, H., Wang, Z., Cai, H., Lu, Z., Li, Y., Du, M., Huang, G., Wang, C., Chen, X., et al. (2017). A STING-activating nanovaccine for cancer immunotherapy. Nat. Nanotechnol. *12*, 648–654. https://doi.org/10.1038/nnano.2017.52.
26. Shae, D., Baljon, J.J., Wehbe, M., Christov, P.P., Becker, K.W., Kumar, A., Suryadevara, N., Carson, C.S., Palmer, C.R., Knight, F.C., et al. (2020). Co-delivery of peptide neoantigens and stimulator of interferon genes agonists enhances response to cancer vaccines. ACS Nano *14*, 9904–9916. https://doi.org/10.1021/acsnano.0c02765.
27. Ge, J., Lei, J., and Zare, R.N. (2012). Protein–inorganic hybrid nanoflowers. Nat. Nanotechnol. *7*, 428–432. https://doi.org/10.1038/nnano.2012.80.
28. Cui, J., and Jia, S. (2017). Organic–inorganic hybrid nanoflowers: A novel host platform for immobilizing biomolecules. Coord. Chem. Rev. *352*, 249–263. https://doi.org/10.1016/j.ijbiomac.2019.05.206.
29. Al Zoubi, W., Kamil, M.P., Fatimah, S., Nashrah, N., and Ko, Y.G. (2020). Recent advances in hybrid organic-inorganic materials with spatial architecture for state-of-the-art applications. Prog. Mater. Sci. *112*, 100663. https://doi.org/10.1016/j.pmatsci.2020.100663.
30. Liang, K., Ricco, R., Doherty, C.M., Styles, M.J., Bell, S., Kirby, N., Mudie, S., Haylock, D., Hill, A.J., Doonan, C.J., and Falcaro, P. (2015). Biomimetic mineralization of metal-organic frameworks as protective coatings for biomacromolecules. Nat. Commun. *6*, 7240. https://doi.org/10.1038/ncomms8240.
31. Kumar, R., Srivastava, V., Baindara, P., and Ahmad, A. (2022). Thermostable vaccines: an innovative concept in vaccine development. Expert Rev. Vaccines *21*, 811–824. https://doi.org/10.1080/14760584.2022.2053678.
32. Wang, G., Cao, R.-Y., Chen, R., Mo, L., Han, J.-F., Wang, X., Xu, X., Jiang, T., Deng, Y.-Q., Lyu, K., et al. (2013). Rational design of thermostable vaccines by engineered peptide-induced virus self-biomineralization under physiological conditions. Proc. Natl. Acad. Sci. USA *110*, 7619–7624. https://doi.org/10.1073/pnas.1300233110.
33. Wang, G., Li, X., Mo, L., Song, Z., Chen, W., Deng, Y., Zhao, H., Qin, E., Qin, C., and Tang, R. (2012). Eggshell-inspired biomineralization generates vaccines that do not require refrigeration. Angew. Chem. *51*, 10576–10579. https://doi.org/10.1002/anie.201206154.
34. Guo, J., De May, H., Franco, S., Noureddine, A., Tang, L., Brinker, C.J., Kusewitt, D.F., Adams, S.F., and Serda, R.E. (2022). Cancer vaccines from cryogenically silicified tumour cells functionalized with pathogen-associated molecular patterns. Nat. Biomed. Eng. *6*, 19–31. https://doi.org/10.1038/s41551-021-00795-w.
35. Wang, S., Ni, D., Yue, H., Luo, N., Xi, X., Wang, Y., Shi, M., Wei, W., and Ma, G. (2018). Exploration of antigen induced CaCO3 nanoparticles for therapeutic vaccine. Small *14*, 1704272. https://doi.org/10.1002/smll.201704272.
36. Wang, C., Wang, X., Zhang, W., Ma, D., Li, F., Jia, R., Shi, M., Wang, Y., Ma, G., and Wei, W. (2022). Shielding ferritin with a biomineralized shell enables efficient modulation of tumor microenvironment and targeted delivery of diverse therapeutic agents. Adv. Mater. *34*, 2107150. https://doi.org/10.1002/adma.202107150.
37. Lv, M., Chen, M., Zhang, R., Zhang, W., Wang, C., Zhang, Y., Wei, X., Guan, Y., Liu, J., Feng, K., et al. (2020). Manganese is critical for antitumor immune responses via cGAS-STING and improves the efficacy of clinical immunotherapy. Cell Res. *30*, 966–979. https://doi.org/10.1038/s41422-020-00395-4.
38. Wang, C., Guan, Y., Lv, M., Zhang, R., Guo, Z., Wei, X., Du, X., Yang, J., Li, T., Wan, Y., et al. (2018). Manganese increases the sensitivity of the cGAS-STING pathway for double-stranded DNA and is required for the host defense against DNA viruses. Immunity *48*, 675–687.e7. https://doi.org/10.1016/j.immuni.2018.03.017.
39. Lee, S.W., Cheon, S.A., Kim, M.I., and Park, T.J. (2015). Organic–inorganic hybrid nanoflowers: types, characteristics, and future prospects. J. Nanobiotechnol. *13*, 54. https://doi.org/10.1186/s12951-015-0118-0.
40. Huang, Z., Zheng, L., Feng, F., Chen, Y., Wang, Z., Lin, Z., Lin, X., and Weng, S. (2018). A Simple and Effective Colorimetric Assay for Glucose Based on MnO_2 Nanosheets. Sensors *18*, 2525. https://doi.org/10.3390/s18082525.
41. Koshy, S.T., Cheung, A.S., Gu, L., Graveline, A.R., and Mooney, D.J. (2017). Liposomal delivery enhances immune activation by STING agonists for cancer immunotherapy. Adv. Biosyst. *1*, 1600013. https://doi.org/10.1002/adbi.201600013.
42. Lv, X., Huang, J., Min, J., Wang, H., Xu, Y., Zhang, Z., Zhou, X., Wang, J., Liu, Z., and Zhao, H. (2023). Multi-signaling pathway activation by pH responsive manganese particles for enhanced vaccination. J. Control. Release *357*, 109–119. https://doi.org/10.1016/j.jconrel.2023.01.078.
43. Zhao, H., Xu, J., Li, Y., Guan, X., Han, X., Xu, Y., Zhou, H., Peng, R., Wang, J., and Liu, Z. (2019). Nanoscale coordination polymer based nanovaccine for tumor immunotherapy. ACS Nano *13*, 13127–13135. https://doi.org/10.1021/acsnano.9b05974.
44. Conlon, J., Burdette, D.L., Sharma, S., Bhat, N., Thompson, M., Jiang, Z., Rathinam, V.A.K., Monks, B., Jin, T., Xiao, T.S., et al. (2013). Mouse, but not human STING, binds and signals in response to the vascular disrupting agent 5, 6-dimethylxanthenone-4-acetic acid. J. Immunol. *190*, 5216–5225. https://doi.org/10.4049/jimmunol.1300097.
45. Najibi, A.J., Dellacherie, M.O., Shih, T.Y., Doherty, E.J., White, D.A., Bauleth-Ramos, T., Stafford, A.G., Weaver, J.C., Yeager, C.D., Seiler, B.T., et al. (2022). Scaffold Vaccines for

Generating Robust and Tunable Antibody Responses. Adv. Funct. Mater. *32*, 2110905. https://doi.org/10.1002/adfm.202110905.

46. Shih, T.-Y., Najibi, A.J., Bartlett, A.L., Li, A.W., and Mooney, D.J. (2021). Ultrasound-triggered release reveals optimal timing of CpG-ODN delivery from a cryogel cancer vaccine. Biomaterials *279*, 121240. https://doi.org/10.1016/j.biomaterials.2021.121240.
47. Kang, X., Li, Y., Zhao, Y., and Chen, X. (2022). Overcoming Aging-Associated Poor Influenza Vaccine Responses with CpG 1018 Adjuvant. Vaccines *10*, 1894. https://doi.org/10.3390/vaccines10111894.
48. Fang, L., Zhao, Z., Wang, J., Zhang, P., Ding, Y., Jiang, Y., Wang, D., and Li, Y. (2020). Engineering autologous tumor cell vaccine to locally mobilize antitumor immunity in tumor surgical bed. Sci. Adv. *6*, eaba4024. https://doi.org/10.1126/sciadv.aba4024.
49. Zhang, J., Chen, C., Li, A., Jing, W., Sun, P., Huang, X., Liu, Y., Zhang, S., Du, W., Zhang, R., et al. (2021). Immunostimulant hydrogel for the inhibition of malignant glioma relapse post-resection. Nat. Nanotechnol. *16*, 538–548. https://doi.org/10.1038/s41565-020-00843-7.
50. O'Donnell, J.S., Hoefsmit, E.P., Smyth, M.J., Blank, C.U., and Teng, M.W.L. (2019). The Promise of Neoadjuvant Immunotherapy and Surgery for Cancer Treatment. Clin. Cancer Res. *25*, 5743–5751. https://doi.org/10.1158/1078-0432.CCR-18-2641.
51. Kim, J., Li, W.A., Choi, Y., Lewin, S.A., Verbeke, C.S., Dranoff, G., and Mooney, D.J. (2015). Injectable, spontaneously assembling, inorganic scaffolds modulate immune cells in vivo and increase vaccine efficacy. Nat. Biotechnol. *33*, 64–72. https://doi.org/10.1038/nbt.3071.
52. Barlow, A.L., Macleod, A., Noppen, S., Sanderson, J., and Guérin, C.J. (2010). Colocalization analysis in fluorescence micrographs: verification of a more accurate calculation of pearson's correlation coefficient. Microsc. Microanal. *16*, 710–724. https://doi.org/10.1017/S143192761009389X.
53. Xu, J., Lv, J., Zhuang, Q., Yang, Z., Cao, Z., Xu, L., Pei, P., Wang, C., Wu, H., Dong, Z., et al. (2020). A general strategy towards personalized nanovaccines based on fluoropolymers for post-surgical cancer immunotherapy. Nat. Nanotechnol. *15*, 1043–1052. https://doi.org/10.1038/s41565-020-00781-4.
54. Wu, Y., Li, Q., Yan, Y., Hao, Y., Wang, C., Liu, B., Zhu, Y., Liu, Z., and Feng, L. (2024). Gel-mediated recruitment of conventional type 1 dendritic cells potentiates the therapeutic effects of radiotherapy. Biomaterials *305*, 122470. https://doi.org/10.1016/j.biomaterials.2024.122470.
55. Li, Q., Dong, Z., Cao, Z., Lei, H., Wang, C., Hao, Y., Feng, L., and Liu, Z. (2023). A General Biomineralization Strategy to Synthesize Autologous Cancer Vaccines with cGAS-STING Activating Capacity for Postsurgical Immunotherapy. ACS Nano *17*, 10496–10510. https://doi.org/10.1021/acsnano.3c01404.
56. Lv, X., Huang, J., Min, J., Wang, H., Xu, Y., Zhang, Z., Zhou, X., Wang, J., Liu, Z., and Zhao, H. (2023). Multi-signaling pathway activation by pH responsive manganese particles for enhanced vaccination. J. Control. Release *357*, 109–119. https://doi.org/10.1016/j.jconrel.2023.01.078.
57. Yang, Z., Zhu, Y., Dong, Z., Li, W., Yang, N., Wang, X., Feng, L., and Liu, Z. (2021). Tumor-killing nanoreactors fueled by tumor debris can enhance radiofrequency ablation therapy and boost antitumor immune responses. Nat. Commun. *12*, 4299. https://doi.org/10.1038/s41467-021-24604-9.

STAR★METHODS

KEY RESOURCES TABLE

REAGENT or RESOURCE	SOURCE	IDENTIFIER
Antibodies		
anti-mouse PD-1	BioXcell	Cat# BE0146; RRID: AB_10949053
Anti-CD3-FITC	Biolegend	Cat# 100204; RRID: AB_ 312660
anti-CD8-APC	Biolegend	Cat# 100712; RRID: AB_312751
anti-CD45-PerCP	Biolegend	Cat# 103130; RRID: AB_893343
anti-FITC-CD11c	Biolegend	Cat# 117306; RRID: AB_313775
anti-CD80-APC	Biolegend	Cat# 104714; RRID: AB_313135
anti-CD80-PE/Cyanine7	Biolegend	Cat# 104734; RRID: AB_2563112
anti-SIINFEKL-H-2Kb-PE	Biolegend	Cat# 141603; RRID: AB_10897938
anti-IFN-γ-PE	Biolegend	Cat# 505808; RRID: AB_315401
anti-MHC class II-APC	Biolegend	Cat# 107614; RRID: AB_313329
anti-CD16/32	Biolegend	Cat# 101302; RRID: AB_312800
H-2K(b)/SIINFEKL Tetramer	HELIXGEN	Cat# HG08T14028
Chemicals, peptides, and recombinant proteins		
Manganese chloride tetrahydrate	Aladdin	Cat# M140867
Sodium phosphate dodecahydrate	Aladdin	Cat# S112445
Ovalbumin	Sigma-Aldrich	Cat# A5503
Heparin sodium	Solarbio	Cat# H8060
Bovine Serum Albumin	Biosharp	Cat# BS114
Transferrin	Yuanye	Cat# S12027
CpG-ODN 1826	InvivoGen	Cat# vac-1826-1
Thiazolyl blue tetrazolium bromide	Macklin	Cat# T818538
Red Blood Cell Lysis Buffer	Solarbio	Cat# R1010
Dulbecco's Modified Eagle Medium (DMEM) culture medium	Cytiva	Cat# SH30243.01
Roswell Park Memorial Institute (RPMI) 1640 culture medium	Cytiva	Cat# SH30027.01
Penicillin/Streptomycin	Cytiva	Cat# SV30010
Fetal Bovine Serum	Inner Mongolia Opcel Biotechnology Co., Ltd.	Cat# BS-1102
Critical commercial assays		
IFN-β ELISA kits	R&D Systems	Cat# DY8234-05
TNF-α ELISA kits	Thermo Fisher Scientific	Cat# 88-7324-88
IL-6 ELISA kits	Thermo Fisher Scientific	Cat# 88-7064-88
Experimental models: Cell lines		
DC2.4 cells	A gift from Prof. C. Wang, Soochow University	N/A
B16-OVA cells	A gift from Prof. R. Peng, Soochow University	N/A
B16-F10 cells	American Type Culture Collection	N/A
CT26 cells	Cell Bank of Shanghai Institutes for Biological Sciences, Chinese Academy of Sciences	N/A
NIH-3T3 cells	Cell Bank of Shanghai Institutes for Biological Sciences, Chinese Academy of Sciences	N/A
293-Dual HEK mSTING cells	InvivoGen	Cat# 293d-mstg

(*Continued on next page*)

Continued

REAGENT or RESOURCE	SOURCE	IDENTIFIER
Experimental models: Organisms/strains		
Mouse: BALB/c	Cavens Laboratory Animal (Changzhou, China)	N/A
Mouse: C57BL/6	Cavens Laboratory Animal (Changzhou, China)	N/A
Software and algorithms		
GraphPad Prism (version 8.0)	GraphPad Software	https://www.graphpad.com
FlowJo (version 10.8.1)	BD Biosciences	https://www.flowjo.com
ImageJ (version 1.50)	National Institutes of Health	https://imagej.net

RESOURCE AVAILABILITY

Lead contact

Further information and requests for resources and reagents should be directed to and will be fulfilled by the lead contact, Liangzhu Feng (lzfeng@suda.edu.cn).

Materials availability

This study did not generate new unique reagents.

Data and code availability

All data needed to evaluate the conclusion of this work are presented in the paper and the supplemental information.

This paper does not report original code.

Any additional information required to reanalyze the data reported in this paper is available from the lead contact upon request.

EXPERIMENTAL MODEL AND STUDY PARTICIPANT DETAILS

Cell lines

DC2.4 cells and CT26 cells were cultured in Roswell Park Memorial Institute (RPMI) 1640 culture medium. B16-OVA cells, B16-F10 cells and NIH-3T3 cells were cultured in Dulbecco's Modified Eagle Medium (DMEM) culture medium. The complete cell culture media were supplemented with 10% FBS and 1% penicillin/streptomycin, and the cells were incubated at 37°C in a humidified atmosphere containing 5% CO_2. 293-Dual HEK mSTING cells were cultured in complete DMEM culture medium following the manufacturer's protocol. BMDCs were prepared from bone marrow cells isolated from the thigh and shin bones of healthy C57BL/6 mice following the standard preparation method.[51] Non-adherent and loosely adherent cells (>70% $CD11c^+$, 6%–13% $CD80^+CD86^+$) were collected for further experiments.

Animals

Female C57BL/6 and BALB/c mice (6–8 weeks old) were purchased from Changzhou Cavens Laboratory Animal Co., Ltd. All animal experiments were performed according to ethical compliance approved by the Institutional Animal Care and Use Committee of Soochow University (Approval Number: SYXK(Su)2021-0073). To establish s.c. tumors, 1×10^6 B16-F10 cells or 2×10^6 B16-OVA cells were suspended in 50 μL of PBS and subcutaneously inoculated into the right ventral flank of C57BL/6 mice.

METHOD DETAILS

Synthesis and characterization of OVA@MnP

$MnCl_2$ aqueous solution (0.5 M, 10 μL) was added to OVA aqueous solution (1 mL) at different concentrations under vigorous stirring for 5 min before Na_3PO_4 aqueous solution (0.33 M, 10 μL) was added to the mixture. Fifteen minutes later, the white turbid reaction mixture was collected by centrifugation at 14800 rpm for 5 min, and the obtained OVA@MnP was further washed three times with deionized water via centrifugation and stored at 4°C for further experiments. BSA (1 mL, 10 mg/mL), transferrin (1 mL, 10 mg/mL) and heparin sodium (1 mL, 100 μg/mL) were used as templates to prepare the corresponding nanoflowers via the same procedures as mentioned above.

The hydrodynamic size of OVA@MnP suspended in deionized water was measured by a Zetasizer (Nano ZS90, Malvern). The morphology of OVA@MnP mounted on an SEM stub with a conductive adhesive and coated with an ultrathin layer of gold was characterized by SEM (G500 and Supra55, Zeiss) at 10 kV. The TEM image and elemental composition of OVA@MnP were characterized by using a TEM (TALOS 200X, Sigma) instrument equipped with HAADF imaging and energy dispersive X-ray spectroscopy (EDX). X-ray diffraction (XRD) patterns of OVA@MnP after lyophilization were recorded by using an X-ray diffractometer (Empyrean, Malvern Panalytical).

The Mn^{2+} content of OVA@MnP was quantified by a sodium periodate oxidation colorimetric assay[40] and inductively coupled plasma-mass spectrometry (ICP-MS, Jena, PlasmaQuant MS). The acidity neutralization capability of OVA@MnP was measured by a pH microsensor

(Presens). To characterize the stability, OVA@MnP was first subjected to different treatments, including sterilization by a high-pressure steam sterilizer (GR60DP, Zealway), lyophilization by freeze drying (Freezone, Labconco) or storage in a refrigerator (−80°C), room temperature (25°C) or drying oven (60°C) for up to 6 months before being examined by SEM.

In vitro cell experiments

To test the biocompatibility of OVA@MnP, DC2.4 cells were first cultured in 96-well plates at a density of 1×10^4 cells/well for 24 h. Then, they were incubated with OVA@MnP at various concentrations for another 24 h before their cell viability was determined via the standard 2,5-diphenyltetrazolium bromide (MTT) assay according to the vendor's protocol.

To test the intracellular trafficking profiles of OVA@MnP, OVA was first labeled with FITC-*N*-hydroxysuccinimide (NHS) (Qiyuebio) following the manufacturer's protocol and purified by running a G-25 column (Sephadex) before being used to guide the formation of OVA@MnP as previously described. Then, DC2.4 cells preseeded in a 12-well plate containing sterilized glass slides (1×10^5 cells/well) were incubated with FITC-OVA and FITC-OVA@MnP for 6 h at 37°C. Then, the treated cells were washed twice with PBS before being subjected to fresh medium containing commercial LysoTracker red (200 nM, Invitrogen) for another 1 h before being imaged by using a confocal microscope (LSM 800, Zeiss). After that, the Pearson correlation coefficients of the recorded images were analyzed by using ImageJ software according to a previously reported method.[52] In brief, the single cell images of the merged channel were first split to corresponding red channel image and green channel images using ImageJ software. Then, the fluorescence intensity of each pixel in both red and green channel images was recorded and analyzed by the JACoP plugin of ImageJ software to obtain corresponding Pearson correlation coefficients according to the following Equation 1:

$$Pearson\ correlation\ coefficients = \frac{\sum (R_i - R_{aver}) \cdot (G_i - G_{aver})}{\sqrt{\sum (R_i - R_{aver})^2 \cdot \sum (G_i - G_{aver})^2}} \quad \text{(Equation 1)}$$

where R_i is the intensity in red channel, G_i is the intensity in green channel, R_{aver} is the average intensity in red channel, and G_{aver} is the average intensity in green channel.

To test the effect of OVA@MnP treatment on DC maturation, BMDCs (5×10^5 cells/well) were treated with OVA, Mn^{2+} + OVA or OVA@MnP (Mn = 3.5 μg/mL; OVA = 13.2 μg/mL) for 24 h in nontreated 24-well plates. Then, the supernatant of each well was harvested for the detection of IFN-β, TNF-α and IL-6 by using the corresponding ELISA kit, while the cells were stained with the corresponding fluorescence antibodies to determine their maturation (anti-CD11c-FITC, anti-CD80-PE/Cyanine7, anti-MHC-II-APC) and antigen cross-presentation status (anti-CD11c-FITC, anti-SIINFEKL-H-2Kb-PE) via flow cytometry (BD Accruit TM C6 Plus).

To test the capacity of OVA@MnP to stimulate the cGAS-STING pathway, 293-Dual mSTING reporter cells (ISG-SEAP/KI-[IFN-β]Lucia) were first transfected with 500 ng of the cGAS plasmid by using Lipofectamine 3000 (Thermo Fisher) according to the manufacturer's instructions. cGAS-transfected 293-Dual mSTING reporter cells received the same treatments as mentioned above for 24 h. Next, the supernatant of each well was collected and incubated with coelenterazine (InvivoGen, Catalog: rep-qlc1) following the manufacturer's protocol, followed by bioluminescence intensity recording using a microreader (Variskan, Thermo).

In vivo animal experiments

Female C57BL/6 and BALB/c mice (6–8 weeks old) were purchased from Changzhou Cavens Laboratory Animal Co., Ltd. All animal experiments were performed according to ethical compliance approved by the Institutional Animal Care and Use Committee of Soochow University (Approval Number: SYXK(Su)2021-0073). To establish s.c. tumors, 1×10^6 B16-F10 cells or 2×10^6 B16-OVA cells were suspended in 50 μL of PBS and subcutaneously inoculated into the right ventral flank of C57BL/6 mice.

To evaluate the *in vivo* vaccination capacity of OVA@MnP, 4 groups of healthy C57BL/6 mice received the following injections: G1, saline; G2, OVA; G3, CpG-ODN + OVA; G4, Mn^{2+} + OVA; and G5, OVA@MnP, where the doses of OVA, Mn^{2+} and CpG were 5.6 mg/kg, 1.5 mg/kg and 1 mg/kg, respectively. The iLNs were excised 7 days after the last immunization and then minced to prepare single-cell suspensions according to a previously described protocol.[53] After staining with anti-CD11c-FITC, anti-CD80-APC and anti-SIINFEKL/H-2Kb-PE, these cells were subjected to flow cytometric analysis of the abundance, maturation status and cross-presentation profiles of DCs. In addition, the spleens of these mice were collected to prepare single-cell suspensions for subsequent flow cytometric analysis according to a previously reported protocol.[53] These cells were stained with anti-CD45-PerCP, anti-CD3-FITC, anti-CD8-APC, and anti-SIINFEKL-MHC-I tetramer-PE to analyze the SIINFEKL-MHC-I tetramer$^+$CD8$^+$ T cells.

To examine the cellular responses, 1×10^6 splenocytes/well were pulsed with SIINFEKL peptide (GenScript, 100 μg/mL) and monensin (BD Bioscience, 2 μM) for 6 h. Then, these cells were collected by centrifugation and stained with anti-CD45-PerCP, anti-CD3-FITC, and anti-CD8-APC, followed by 1 h of cell fixation with intracellular (IC) fixation buffer (Thermo Fisher) at room temperature. The cells were washed and permeabilized with commercial permeabilization buffer (Thermo Fisher) and stained with anti-IFN-γ-PE antibodies before being subjected to flow cytometry to analyze the percentage of OVA-specific IFN-γ-expressing CD8$^+$ T cells. An ELISPOT kit (Dakewe, Catalog: 2210005) was used to incubate 5×10^5 splenocytes/well with 10 μg/well SIINFEKL peptides at 37°C for 24 h, and the results were analyzed according to the manufacturer's instructions.

To evaluate the prophylactic efficacy of OVA@MnP, 25 mice were randomly divided into 5 groups and subjected to the following treatments: G1, saline; G2, OVA; G3, CpG-ODN + OVA; G4, Mn^{2+} + OVA; and G5, OVA@MnP (OVA = 5.6 mg/kg, Mn^{2+} = 1.5 mg/kg and

CpG = 1 mg/kg). The dosages of Mn^{2+}, OVA, and CpG-ODNs were determined according to previous studies.[37,53–56] The different vaccines were s.c. injected into the left ventral flank of the mice on days 0, 7, and 14. Seven days after the final vaccination, the mice were s.c. inoculated with 2×10^6 B16-OVA cells into the right ventral flank of C57 mice, and their tumor volumes were recorded by recording tumor length and width using a digital caliper. To evaluate the therapeutic efficacy of OVA@MnP, C57BL/6 mice were s.c. injected with 2×10^6 B16-OVA cells in the right ventral flank 4 days before vaccination, while different vaccines were s.c. injected into the left ventral flank on day 0, day 7 and day 14 at the aforementioned doses. The tumor volume was recorded using a digital caliper and calculated as V = length × width × width/2. Mice were euthanized when the tumor volume exceeded 1500 mm^3.

To prepare the autologous cancer vaccine, B16-F10 melanoma and CT26 colon cancer-bearing C57BL/6 mice were anesthetized, and 95% of their tumor mass was surgically excised when the tumor volume reached 100 mm^3. Then, these tumor masses were first prepared into single-cell suspensions through enzymatic digestion with collagenase I (1.5 mg/mL, Biofroxx), collagenase IV (1.5 mg/mL, Biofroxx) and hyaluronidase (1 mg/mL, Biofroxx) and RBC lysis. After that, the obtained B16 tumor single-cell suspensions were deactivated by heating at 75°C for 2 h before being dissolved in urea solution (8 M) with sonication for 5 min. Then, the TCLs (protein = 1 mg/mL, 500 μL) were annealed at 95°C to guide the formation of TCL@MnP by following the aforementioned biomineralization procedure.

To evaluate the therapeutic efficacy of TCL@MnP combined with anti-PD1 immunotherapy, the resected mice with ~5% remaining tumor mass were randomly divided into four groups and treated as follows: G1, saline; G2, anti-PD-1; G3, TCL@MnP; and G4, TCL@MnP + anti-PD-1. The doses of TCL, Mn^{2+} and anti-PD-1 were 5 mg/kg, 1.5 mg/kg and 1 mg/kg, respectively. The dosages of TCL and anti-PD-1 were determined according to previous studies.[55,57] Vaccines were suspended in 50 μL of saline and s.c. injected into the left ventral flank of mice on day 1, day 8 and day 15, while anti-PD-1 was i.v. administered at 2 and 5 days after each TCL@MnP vaccination. The tumor volume was recorded as previously described.

QUANTIFICATION AND STATISTICAL ANALYSIS

Data were represented as mean values with standard deviation obtained using Graph Pad Prism 8.0. Differences between groups were estimated using the two-tailed Student's t test. When the *p*-value is less than 0.05, indicating a significant difference. Further statistical details, including *n* values, are provided in the figure legends.